A&A 391, 531–545 (2002)
DOI: 10.1051/0004-6361:20020904

Astronomy & Astrophysics

Near-infrared surface photometry of early-type galaxies

S. B. Rembold[1], M. G. Pastoriza[1], J. R. Ducati[1], M. Rubio[2], and M. Roth[3]

[1] Departamento de Astronomia, Instituto de Física, Universidade Federal do Rio Grande do Sul, Av. Bento Gonçalves 9500, CP 15051, 91501-970 Porto Alegre, Brazil
e-mail: rembold@if.ufrgs.br;mgp@if.ufrgs.br;ducati@if.ufrgs.br
[2] Departamento de Astronomía, Universidad de Chile, Casilla 36-D, Santiago, Chile
e-mail: mrubio@das.uchile.cl
[3] Carnegie Institution of Washington, Las Campanas Observatory, Casilla 601, La Serena, Chile
e-mail: mroth@lco.cl

Received 24 April 2002 / Accepted 23 May 2002

Abstract. CCD infrared (JHK_s) photometry was performed on a sample of 10 elliptical and 2 lenticular galaxies. Isophotal parameters, brightness profiles, integrated colors and color gradients are presented. Color gradients found are very weak, showing bluer colors towards the outer regions. The colors of the sample galaxies are compatible with stellar populations like those found in metal-rich clusters of the Galaxy; objects NGC 7192, NGC 7562 and NGC 7619 are compatible with less metal-rich populations. The brightness profile of most galaxies is well described by the $r^{1/4}$ law. The profiles of NGC 1600 and NGC 720 are described by Sérsic's law with $n \sim 1.5$ and $n \sim 1.8$ respectively. The infrared effective radius of the objects studied is typically one half of its counterpart in the B band, which can be an indication that the stellar population that dominates the infrared emission is more concentrated in the central regions. We show that the sample satisfies the Fundamental Plane relation of elliptical galaxies in the infrared, with an rms scatter of 0.20 for J and H and 0.23 for K_s.

Key words. galaxies: elliptical and lenticular, cD – galaxies: stellar content – galaxies: photometry

1. Introduction

Surface photometry of elliptical galaxies has become, in the last decades, a powerful tool to study the structure and general properties of these objects (Kormendy & Djorgovski 1989). A large database on surface photometry, especially in V band, has been produced, and refined techniques of analysis have been employed. For example, the isophote shapes give valuable information about the intrinsic structure of elliptical galaxies, like triaxiality (Bertola 1981); color indices and gradients give information on stellar content and metallicity (Tamura et al. 2000). Brightness profiles have been widely used to construct quantitative parametrizations of early-type systems, as the well-known de Vaucouleurs $r^{1/4}$ law, and the more recent Sérsic's $r^{1/n}$ law. It was found, in several works, that the latter law fits a larger variety of profile shapes (Saraiva et al. 1999).

However, this large quantitative and qualitative analysis is far less established in the infrared bands, a situation that will probably change with the availability of the 2MASS survey. One of the first works analyzing the behavior of infrared scale parameters (R_e, μ_e) was made by Pahre et al. (1998) who, using a large sample of early-type galaxies observed in the optical and in the near-infrared K band, found a variation of the slope of the Fundamental Plane (FP) relation with the wavelength. Mobasher et al. (1999) found similar results observing early-type galaxies in the Coma cluster at K band. There are very few analyses of isophotal parameters in the infrared JHK_s broadbands. It is not well established whether the observed properties of isophotes in the optical region – e.g. twists, Fourier parameters and ellipticity – are connected to its near-IR counterparts. Furthermore, information on $J-H$ and $H-K$ colors and color gradients is available only for a small number of early-type galaxies, although near-infrared colors are crucial to understand the properties of the stellar population and its distribution in these systems.

In order to make more information available on the near-infrared photometric properties of early-type systems, we present in this work detailed infrared surface photometry (JHK_s) analysis for a sample of 12 bright early-type galaxies. For some of them, these are the first near-IR data available. This sample is selected from a larger list of galaxies containing gas and dust (Macchetto et al. 1996; Ferrari et al. 1999), making near-infrared surface photometry important, since it is less affected than the optical by the interstellar medium.

This paper is structured as follows: in Sect. 2, we present the observations and data reduction; in Sect. 3, we present the analysis of the data; in Sect. 4, we present the results of the analysis; in Sect. 5, we discuss the main results; finally Sect. 6 presents the general conclusions.

Send offprint requests to: S. B. Rembold,
e-mail: rembold@if.ufrgs.br

Table 1. Observed galaxies.

Galaxy	α	δ	Morph.	v_r (km s^{-1})	B_T^0	A_B	Dist. (Mpc)
IC 5105	21 24 22.4	−40 32 06	E5	5407 ± 13	12.42	0.15	80.61
NGC 596	01 32 52.1	−07 01 55	E0/S0	1876 ± 11	11.66	0.16	29.57
NGC 636	01 39 06.5	−07 30 46	E1	1860 ± 6	12.22	0.11	28.83
NGC 720	01 53 00.4	−13 44 18	E5	1745 ± 7	11.13	0.07	25.89
NGC 1400	03 39 31.0	−18 41 22	S0	558 ± 14	11.89	0.28	7.16
NGC 1453	03 46 27.2	−03 58 09	E0	3886 ± 6	12.26	0.45	60.23
NGC 1600	04 31 39.9	−05 05 10	E4	4688 ± 8	11.83	0.19	72.35
NGC 7192	22 06 50.3	−64 18 56	S0	2904 ± 15	12.23	0.15	41.87
NGC 7562	23 15 57.3	+06 41 16	E2	3608 ± 5	12.37	0.45	57.29
NGC 7619	23 20 14.4	+08 12 22	E3	3762 ± 5	11.93	0.35	60.05
NGC 7626	23 20 42.3	+08 13 02	E1	3405 ± 4	12.06	0.31	53.99
NGC 7796	23 58 59.7	−55 27 23	E1	3290 ± 24	12.39	0.04	72.35

2. Observations and data reduction

2.1. The sample

The galaxies presented in this paper have been selected from the sample of elliptical and lenticular galaxies whose ionized gas distribution has been studied by Macchetto et al. (1996); the dust content of IC 5105, NGC 636 and NGC 1600 was studied by Ferrari et al. (1999). We selected those galaxies which were compatible with the observation epoch. The selected galaxies are brighter than $B_T = 13.0$ mag and their morphological types are from *The Revised Shapley-Ames Catalog of Bright Galaxies* (Sandage & Tammann 1987). Table 1 presents morphological types, apparent B_T magnitudes, B extinction and distances (scaled to $H_0 = 65\,\mathrm{km\,s^{-1}\,Mpc^{-1}}$) of the 12 selected objects.

2.2. Observations

The observations were made during 3 nights at the Las Campanas Observatory, Chile, with the infrared camera C40IRC (NICMOS3 HgCdTe detector, 256 × 256 pixels) attached to the 1 m Swope telescope. This instrumental arrange covers, on the sky, an area of 2.5 × 2.5 arcmin^2, with a scale of 0.6 arcsec/pixel. We used the broadband filters J, H and K_s, centered on 1.24, 1.65 and 2.16 μm, with 0.22, 0.30 and 0.33 μm passbands. The H filter is equivalent to the H filter in the CIT/CTIO system; filters J and K_s are variations of standard J and K filters. The J filter is less sensitive to variations in atmospheric water vapor transmission, while K_s does not suffer from background thermal radiation as much as the K filter. For the specific characteristics of these filters, see Persson et al. (1998), who also give infrared photometric data for several stars, allowing us to derive a transformation between systems K and K_s; from a least-square fit, we found $K_s = 1.018\,K - 0.162$.

For all galaxies, we obtained a set of 32 exposures of 30, 30 and 25 s for J, H and K_s respectively, except for NGC 720, NGC 7562 and NGC 7796, where we got only 16 exposures. Images were dithered each 4 exposures. Seeing conditions were fair, varying from 1.05″ to 1.83″, and all nights were photometric. Standard stars from Persson et al. (1998) were also observed, taking 10 exposures of 10 s, with the same dithering conditions used for the galaxies.

2.3. Data reduction

The IRAF reduction package was used to conduct all reduction steps. The images were dark-subtracted and flat-fielded. For each galaxy, the images were median-combined in order to produce its corresponding sky frame. Bad pixels were corrected using CCDMASK and FIXPIX tasks. The final image for each galaxy was obtained combining the sky-subtracted, bad-pixel corrected individual images.

A very pronounced effect in the H images is the formation of *fringes*. The use of twilight sky as a flat-field, with short exposures (~6000 ADU), minimizes this effect in flat-field frames; therefore this correction must be done only in object frames. This correction is made as we calculate the median frame (sky) in each pixel; as the fringing is fixed along the detector, the subtraction of the median extracts this pattern from the science frames.

2.4. Calibration

Photometric calibrations were made using the photometric standards of Persson et al. (1998). IRAF task PHOT was used to perform aperture photometry, giving the instrumental magnitudes of these stars. The adopted photometric transformation to standard magnitudes was

$$m_\lambda^{\mathrm{cal}} = C_\lambda + m_\lambda^{\mathrm{inst}} - k_\lambda X, \quad (1)$$

where C_λ is the zero-point constant for λ filter, k_λ is the atmospheric extinction coefficient and X is the airmass. Like Galaz (2000), we did not use color terms in these equations, since these corrections are of the same order as the instrumental errors. A least-square method was applied to determine the calibration constants C_λ and k_λ for each filter.

The estimated calibration errors are 0.011 mag for J, 0.060 mag for H and 0.059 mag for K_s. While H and K_s errors are of the same order of those expected from photoelectric photometry (Ducati et al. 2001), the J band shows lower values.

3. Analysis

3.1. Ellipse fitting

The main reason for the variations in shape of early-type galaxies is their inclination, but some cases cannot be accounted for by inclination effects and are an indication of intrinsic features, such as triaxiality (Bertola 1981) or gravitational interactions (Binney & Petrou 1985). In order to detect and quantify these effects, we have fitted ellipses to the J, H and K_s isophotes, using the task ELLIPSE in the STSDAS package for IRAF. We determine the position angle (PA) of the isophotes, their ellipticity (ϵ), the Fourier amplitudes of the deviation from perfect ellipses ($\cos 4\theta$ term, B4), as well as the brightness distribution along the isophotes. The behavior of the position angle is related to the shape of the galaxy. A spheroidal galaxy, independent of its inclination, keeps the direction of the semimajor isophotal axis constant; on the contrary, if the galaxy is triaxial, the position angle can rotate (Mihalas & Binney 1981). Interaction among galaxies can also cause isophotal twisting (Bender & Möllenhoff 1987). The presence of dust in the galaxy is related to the behavior of the ellipticity for different wavelengths, and also to the A3, B3 Fourier coefficients: nonzero values are frequently found in regions of strong extinction (Peletier et al. 1990). The B4 Fourier coefficient measures the deviation of the isophote in relation to a perfect ellipse. Positive values imply disky isophotes, while negative values correspond to boxy isophotes. There is evidence that these deviations from elliptical shapes are associated with different physical structures: disky isophotes reflect an intrinsic disk structure, while boxy ones are seen in massive galaxies, possibly indicating interaction phenomena (Kormendy & Djorgovski 1989).

The ellipticity, position angle and A3, B3, A4, B4 coefficients as a function of semimajor axis for all galaxies are shown in Fig. 1. The main characteristics of the objects are:

IC 5105: The ellipticity of this galaxy grows from the center up to ∼0.3; the position angle of semimajor axis is constant for J and H, showing a fluctuation of ∼15° in K_s. It presents slightly boxy isophotes, especially around 10″ (B4 ∼ −0.005).

NGC 596: Presents approximately circular isophotes ($\epsilon \sim 0.1$), for all radii. The position angle of the external isophotes varies about 40° in relation to the central region.

NGC 636: The ellipticity increases up to ∼0.2 in J and K_s, being slightly higher for K_s in the internal regions. The position angle twists more than 30° in J and almost 90° in K_s. This galaxy shows slightly disky external isophotes (B4 ∼ 0.01).

NGC 720: The ellipticity shows a small amount of growth with radius (from 0.2 to 0.5); its position angle is almost constant, and it shows disky isophotes in the inner (∼10″), becoming boxy at the periphery.

NGC 1400: It has low ellipticity isophotes ($\epsilon \sim 0.1$) through the entire semimajor axis, and the position angle presents low variation.

NGC 1453: The ellipticity of this galaxy grows from about 0.1 to 0.2 from the center. The position angle is nearly constant, increasing by ∼10° in the external regions, especially in H and K_s.

NGC 1600: It shows ellipticity of 0.2. The position angle is nearly constant, and the isophotes are boxy from 6″ outward.

NGC 7192: This galaxy presents nearly circular isophotes, which results in the irregular behavior of the position angle values shown in the figure.

NGC 7562: Monotonically increasing ellipticity (0.1 to 0.3) throughout the semimajor axis. The position angle is nearly constant.

NGC 7619: Its ellipticity in the central region is 0.1, reaches a maximum of 0.25 and decreases in the outer regions. The position angle varies slight and monotonically through the radius, and the isophotes are nearly disky.

NGC 7626: Isophotes have low eccentricity (∼0.1). It shows a variation in the position angle (∼50°). In general, its isophotes are disky ($B4 \sim 0.01$).

NGC 7796: Ellipticity and position angle are nearly constant; its isophotes tend to be boxy.

3.2. Luminosity profiles

With the data obtained with the ELLIPSE routine, we built J, H and K_s elliptically averaged brightness profiles along the semimajor axis of the galaxy. In order to find the function that best describes the brightness distribution of the galaxy, we use de Vaucouleurs' ($r^{1/4}$) law, as a first approximation. In terms of surface brightness this law has the following analytical expression:

$$\mu(R) = \mu_e + 8.325\left[\left(\frac{R}{R_e}\right)^{\frac{1}{4}} - 1\right], \quad (2)$$

where R_e (effective radius) is the radius containing one half of the luminosity of the galaxy, and μ_e (effective brightness) is the superficial brightness at $R = R_e$. There have been several studies on the "universality" of the $r^{1/4}$ law, and especially on the insertion of one free parameter in this law – a *shape* parameter. This is made in Sérsic's law (Caon et al. 1993; D'Onofrio et al. 1994), which has the form:

$$\mu(R) = \mu_e + 2.5b_n\left[\left(\frac{R}{R_e}\right)^{\frac{1}{n}} - 1\right]. \quad (3)$$

where $b_n = 0.868n - 0.142$, so that μ_e and R_e keep the same physical meaning as in the de Vaucouleurs law. Having one more free parameter, Sérsic's law naturally should be more successful in fitting observed profiles of early-type galaxies (Saraiva et al. 1999). For a sample of early-type galaxies, Caon et al. (1993) analyzed the physical meaning of the parameter n in the B band, and found that n correlates with the effective radius, in the sense that galaxies with higher n values tend to have higher effective radii. This is an indication that the shape parameter in Sérsic's law has a real physical meaning. Thus, for those profiles that did not fit the de Vaucouleurs law, we applied Sérsic's law. Note that we do not apply Sérsic's law in all profiles, because Sérsic's law is more sensible to the observational errors in the outer regions, and could introduce false structural parameters.

The luminosity profiles of the galaxies of our sample were well fitted by the $r^{1/4}$ law, except those of NGC 720 and

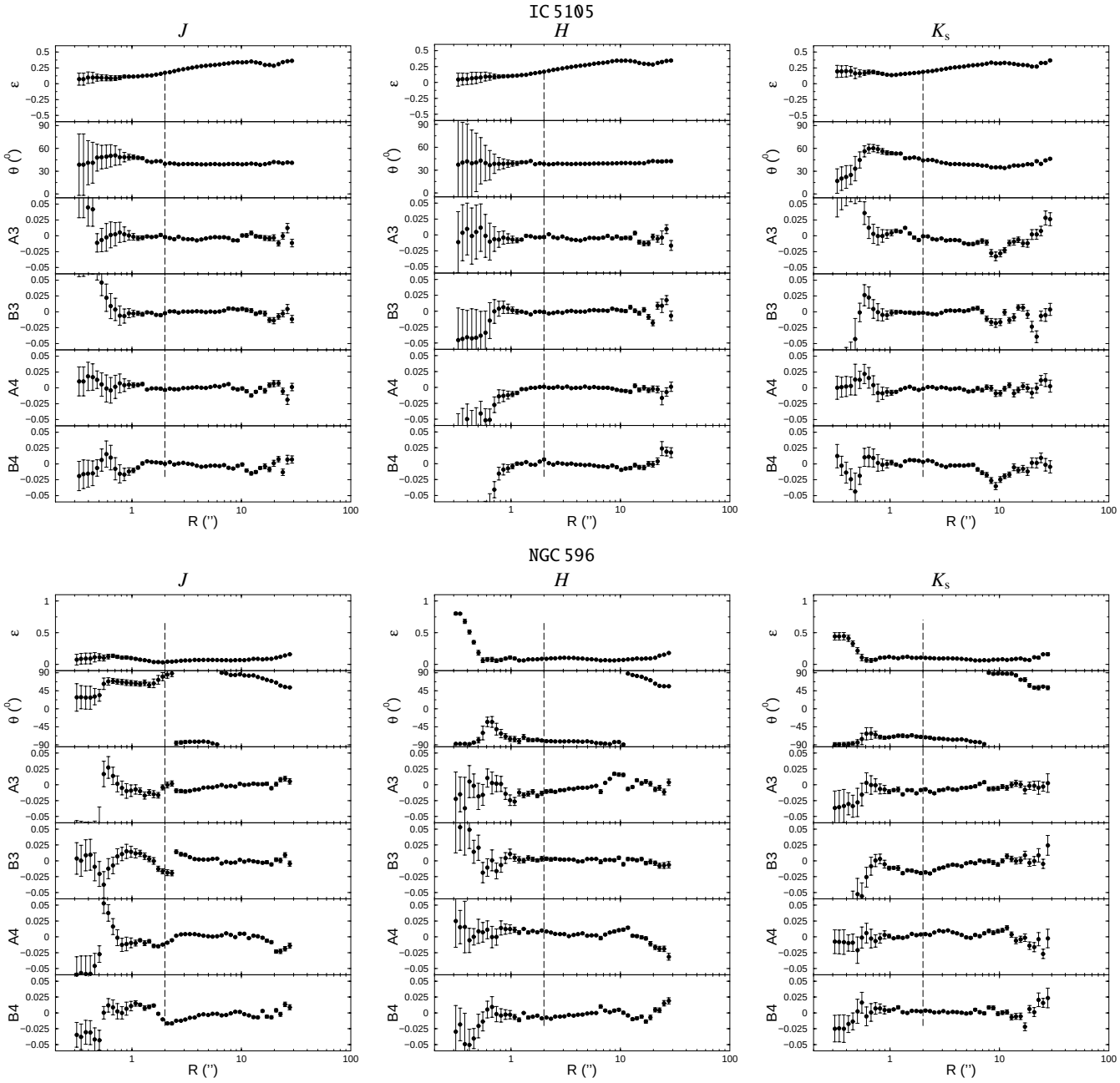

Fig. 1. Isophotal parameters. The vertical line in each graphic represents the region affected by the seeing.

NGC 1600, which fit Sérsic's law. Figure 2 presents the brightness profiles and the best-fitted law for J band; the fittings were made after removing the region affected by seeing. In Fig. 2, the dotted lines represent the difference between observed and fitted profiles, expanded on a scale of 0.25 mag. The profiles in H and K_s show similar characteristics for all the sample galaxies. The parameters R_e and μ_e are listed in Table 2.

3.3. Integrated magnitudes

Integrated magnitudes were calculated with the IRAF task PHOT. Table 3 shows the integrated magnitudes from the aperture photometry, which was performed for 0.2, 0.5 and 1.0 effective radii and for the isophotal radius. The isophotal radius (R_{iso}) is defined as the semimajor axis of the ellipse fitted to a specific limit brightness, called the *isophotal brightness*. The adopted isophotal brightness values were 22.0, 21.5 and 21.0 mag arcsec^{-2} for J, H and K_s respectively (Hunt et al. 1999).

To determine the isophotal radius, we calculated, in the fitted profiles, the radius corresponding to the isophotal brightness. When profiles did not reach the isophotal brightness, what was true for most profiles (marked by "*"), we extrapolated the fitted profile. Table 3 shows the isophotal radii and, for the objects for which extrapolation was used, the difference between the weaker points of the observed profile and the isophotal brightness. We see that the maximum difference between the limit brightness and the isophotal brightness is

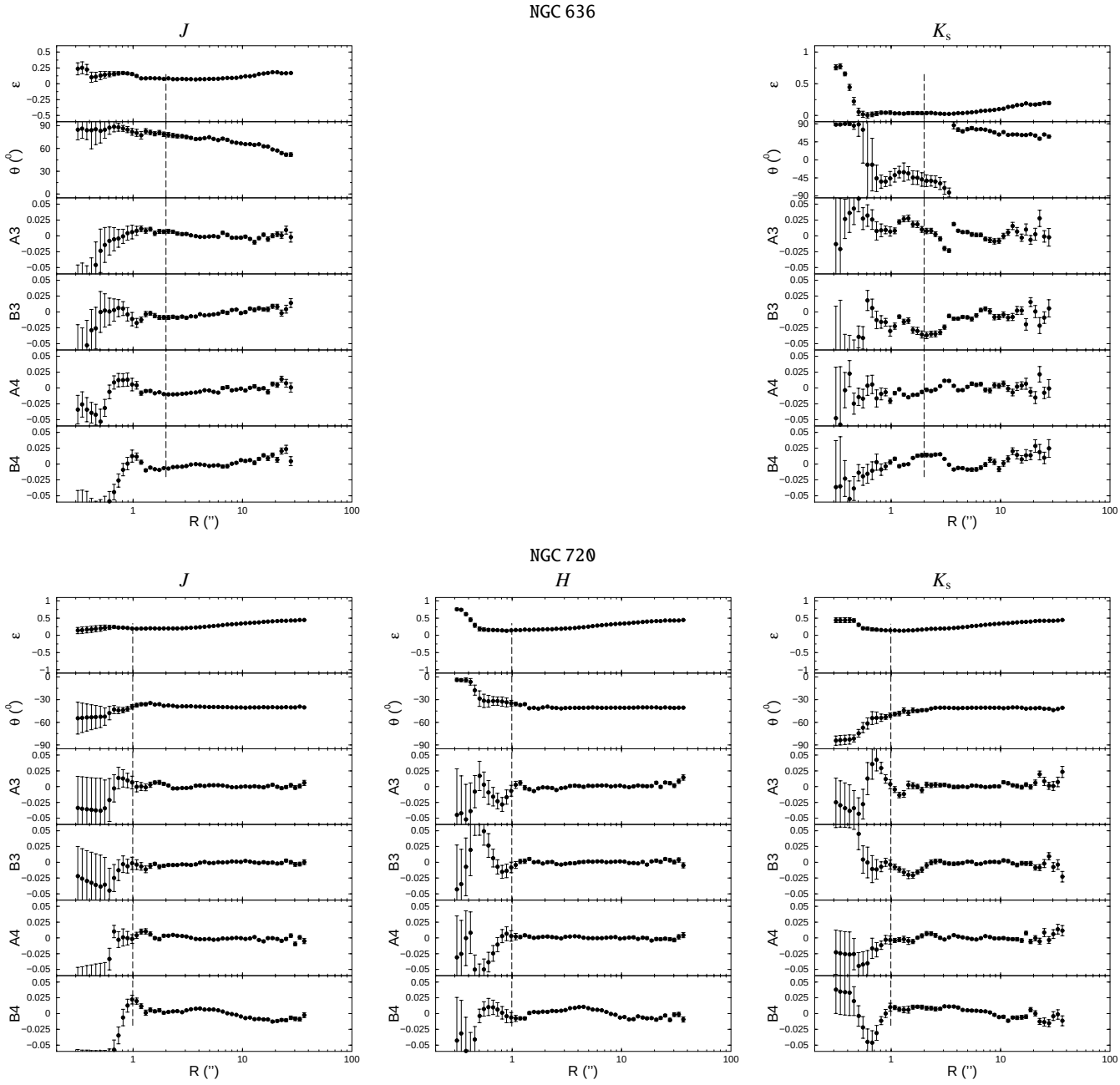

Fig. 1. continued.

about 0.7 mag arcsec^{-2}. So, if we add 1 mag to the isophotal magnitudes adopted, all integrated magnitudes would be obtained without extrapolation. These data (m^*_{iso} and R^*_{iso}) are shown in the last two columns of Table 3. This table also shows the absolute magnitudes, which were calculated using the distances given in Table 1 and corrected for galactic extinction by Schlegel et al. (1998).

3.4. Colors and color gradients

We constructed, through the brightness profiles, the corresponding color profiles. They are represented in Fig. 2, below the brightness profiles. We can see that color gradients are very small, and probably accounted for the observational uncertainties for most of the profiles, albeit showing a systematic tendency to bluer colors in the external region. In some cases, different color profiles do not have the same tendency for the same galaxy (IC 5105 and NGC 1400 present a $J - H$ color tending to redder for the external region, contrary to the other colors; NGC 596 and NGC 7619 present a similar effect for the $H - K_s$ band; galaxy NGC 636 presents a redder $J - K_s$ profile in the external regions). These small near-IR color gradients may reflect the fact that the stellar population that dominates the near-infrared colors is distributed homogeneously throughout the galaxy.

Integrated color were determined from subtraction of the integrated isophotal magnitudes. We present in Fig. 5 a flux ratio diagram from these data, obtained applying $10^{-0.4(\mathrm{color})}$

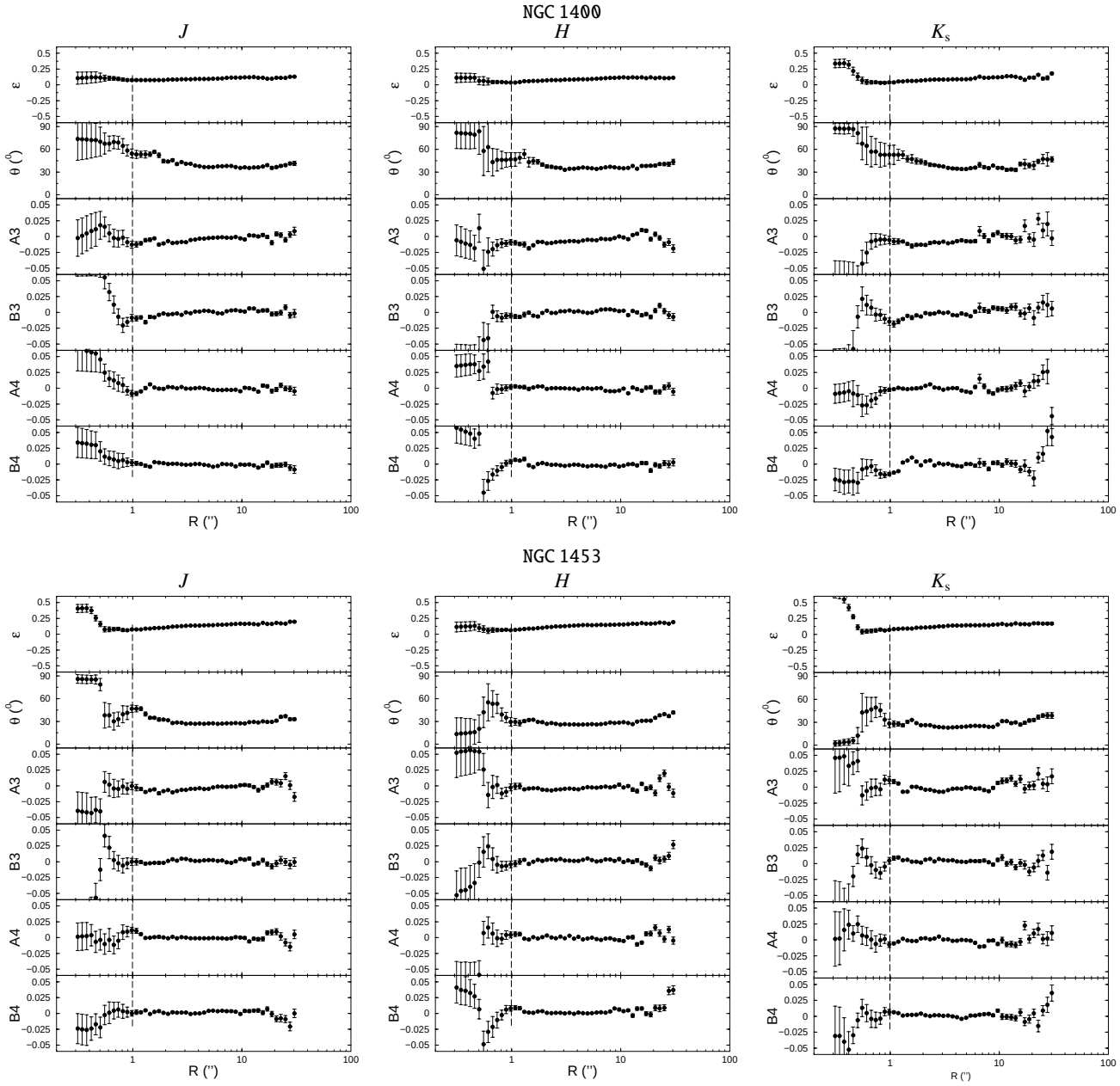

Fig. 1. continued.

to the isophotal colors of the galaxies. This figure also presents the representative region of the sample of E/S0 galaxies from Frogel et al. (1978), whose J/H colors are redder than the average of those observed for our sample. The galaxies NGC 7192, NGC 7562 and NGC 7619 present a very blue J/H color, suggesting that an earlier stellar population may be present in these galaxies (see Sect. 5).

4. Results

4.1. Effective radii analysis

Our sample covers a wide range of effective radii, varying from less than 1 kpc for very compact objects to about 9 kpc for the more extended ones; typical values are between 4 and 6 kpc. The effective brightness is distributed from 18 to 22 mag arcsec^{-2}, being concentrated between 19.0 and 20.5 mag arcsec^{-2}.

Figure 3 (*left*) presents the comparison between effective radii for J, H and K_s. We note little variation of effective radius in the three bands. We have also obtained from de Vaucouleurs (1991), for these galaxies, the effective radii determined from B band photometry, which we compared with those obtained in this paper. The comparison is shown in Fig. 3 (*right*). Despite the considerable dispersion, there is a strong tendency of the effective radii in B to be higher, by a factor of nearly 2, than the corresponding infrared effective radii. This result is compatible with that found by Pahre et al. (1998), who compared effective radii in V and K bands, finding a tendency of effective radii to be higher for shorter wavelengths. Some objects do not

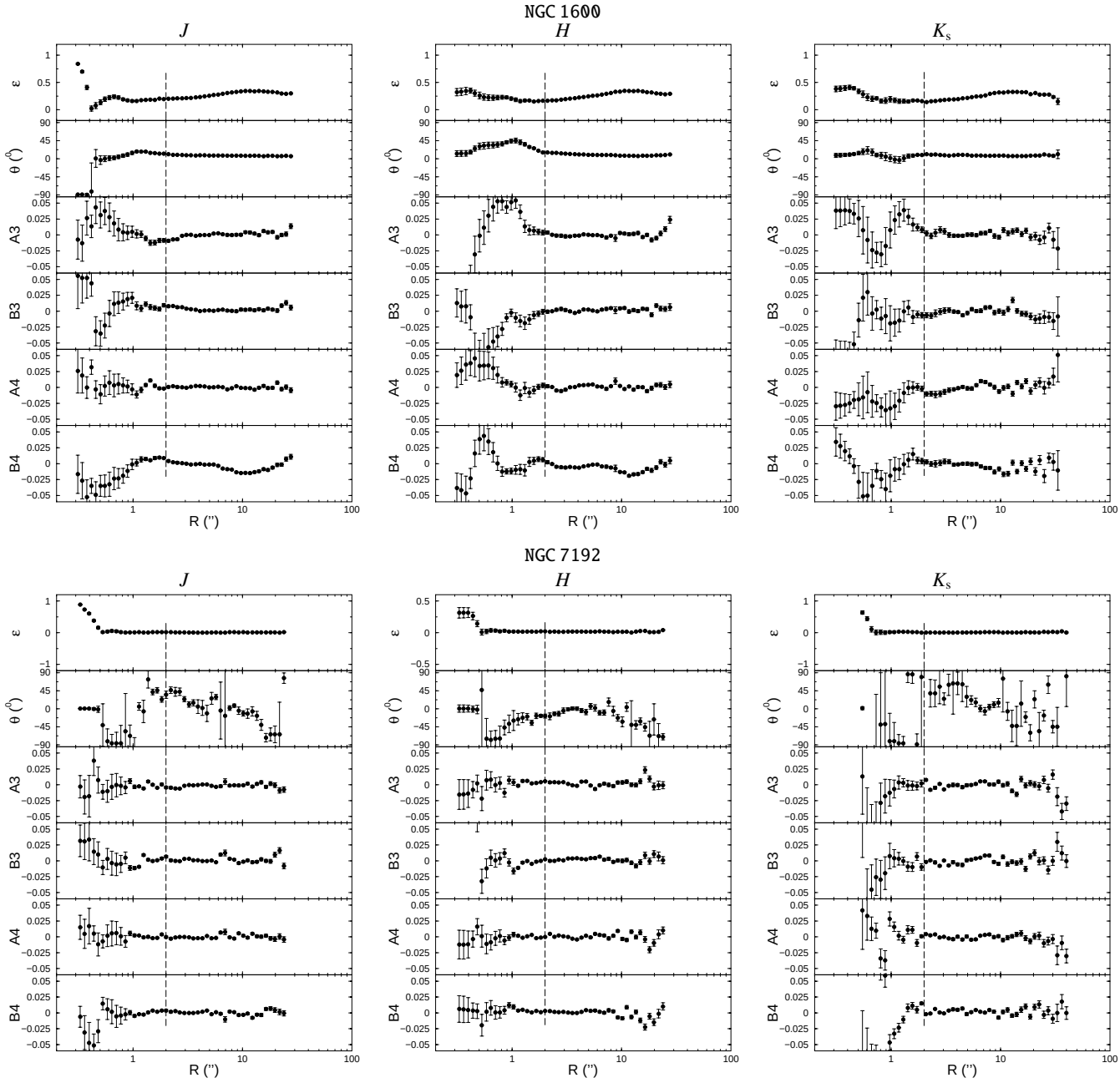

Fig. 1. continued.

follow this tendency; NGC 7562 and IC 5105 are dislocated in the sense of smaller radii in *B*, while NGC 1600 goes in the opposite sense. This effect could be interpreted as being due to differences in the stellar population distribution that contributes to each band. The fact that the *B*-band effective radii are higher than its near-IR counterparts shows that the stellar population that dominates near-IR emission is more concentrated towards the central regions than the bluer one.

4.2. Fundamental plane

One of the most important constraints on early-type galaxy formation and evolution is the existence the three-parametric scaling relation called the Fundamental Plane (FP) relation (Djorgovski & Davis 1987), which is mostly defined for the optical bands. This relation covers a wide range of magnitudes and is, as far as we can see, independent of the environment. The very existence of this relation, which presents a very low scatter, must reflect an important regularity in the evolutive stories of early-type systems, be they dominated by dissipative collapse or not.

From 2.2 μm photometry of elliptical galaxies of the Coma cluster, Mobascher et al. (1999) found that it is possible to define for the same sample the FP in the near-infrared, with a similar dispersion as in the optical bands. Since our work presents *a*) the first near-infrared data available for several objects, *b*) observations in three photometric bands, and *c*) a sample not limited to a specific environment, we found it interesting to

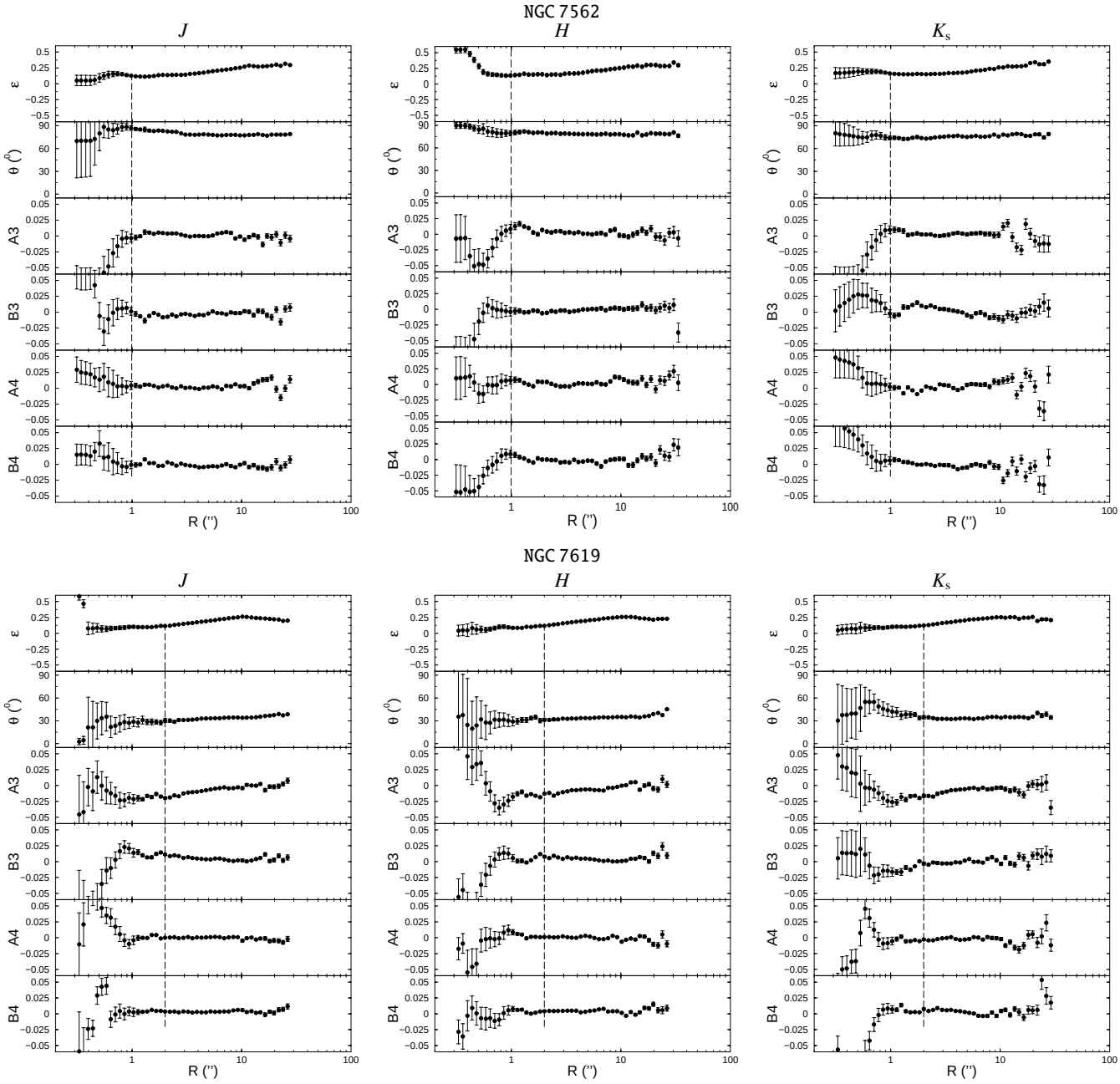

Fig. 1. continued.

analyze the behavior of our sample in relation to the FP. One can express the FP, in terms of the structural parameters and the central velocity dispersion σ, as

$$\log R_e = a \log \sigma + b\,\mu_e + \text{constant}, \quad (4)$$

where a and b are constants to be determined from the fitting.

We have used the central velocity dispersion for our objects from the catalogue of Prugniel & Simien (1996). A least-square method was applied in determining the best-fit regression. We considered the uncertainties in R_e and μ_e as independent quantities, because the correlation coefficient between these quantities is small and largely dependent upon only one point (NGC 1600). We obtained the following relations:

$$\log R_e = (1.44 \pm 0.12) \log \sigma + (0.46 \pm 0.03)\,\mu_e, \text{ for } J \quad (5)$$

$$= (1.60 \pm 0.11) \log \sigma + (0.38 \pm 0.02)\,\mu_e, \text{ for } H \quad (6)$$

$$= (1.42 \pm 0.09) \log \sigma + (0.43 \pm 0.02)\,\mu_e, \text{ for } K_s, \quad (7)$$

where R_e is in parsecs and σ in km s^{-1}.

The a values are in agreement with the average determinations of this constant (Mobasher et al. 1999; Milvang-Jensen 1997). The b values are stable, and near to 0.40. Scodeggio et al. (1998) analyzed the wavelength dependence of the FP parameters for $BVrIHK$ bands, including a correction for completeness of the samples, and discovered that the a values are

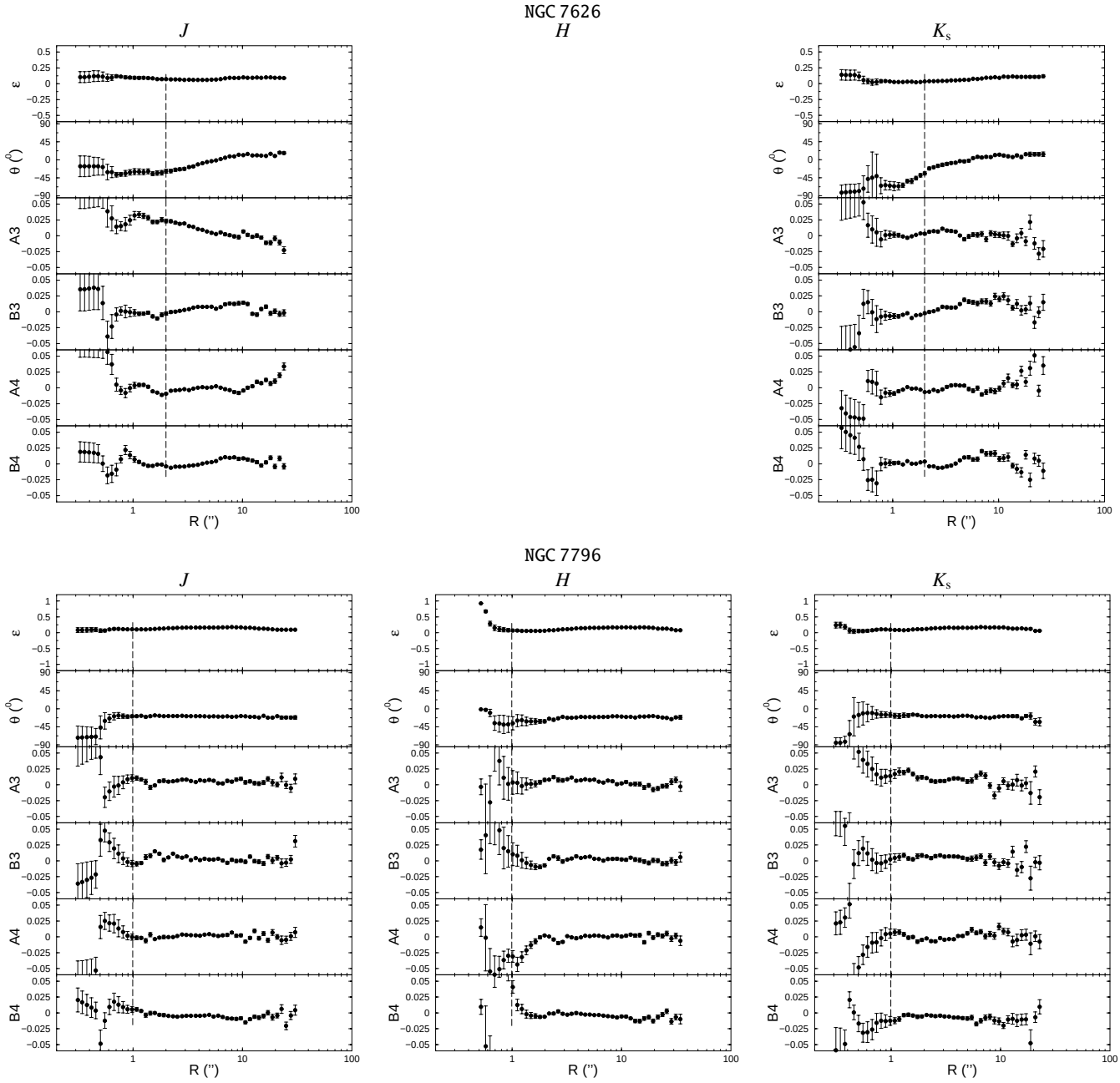

Fig. 1. continued.

strongly wavelength-dependent, varying from 1.13 in *B* to 1.51 to *K*, while the *b* values are constant and near to 0.35. While our *a* values are compatible with those of Scodeggio, the *b* values are higher by nearly 20%.

Figure 4 shows edge-on views of the Fundamental Plane for *J*, *H* and K_s. Although the relationship is built on a small number of point (12 for *J* and K_s, 10 for *H*), that causes the rms scatter of these relations to be relatively high (0.20 dex for *J* and *H*, and 0.23 dex for K_s), the FP is well defined in the three bands. The galaxy mostly off the correlation in the three bands (below the line of correlation) is NGC 1400, which is the most compact galaxy of our sample. We conclude therefore that for our sample of objects from different environments, in a 3-band near-infrared photometry, the Fundamental Plane is well defined.

4.3. Comparison with globular clusters

In order to analyze the integrated stellar population dominating the infrared luminosity of our galaxies, we compared our data with typical infrared colors of globular clusters. Infrared colors of globular clusters from the Magellanic Clouds and from M 31 are represented in Fig. 4. Data for Magellanic Clouds clusters are from Persson et al. (1983); Andromeda Galaxy clusters are from Frogel et al. (1980) (Galactic clusters are distributed in the same region delimited by Andromeda Galaxy cluster; see Aaronson et al. 1978). Magellanic Clouds

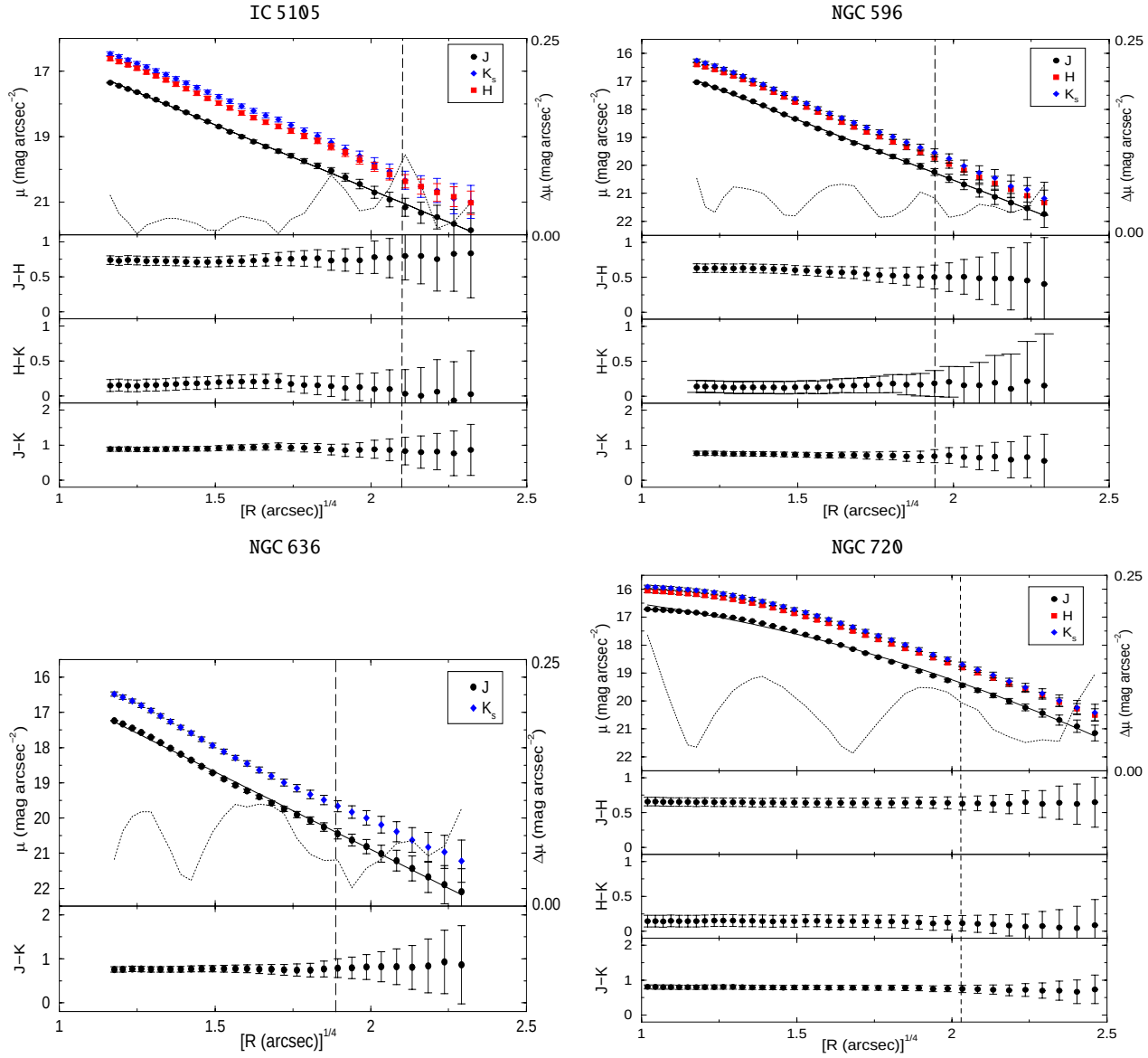

Fig. 2. Brightness and color profiles for the galaxies of our sample. The dashed line in each diagram refers to the effective radius in J band. Dotted curves represented with brightness profiles refer to the difference $\Delta\mu$ between profiles and fittings, expanded to a 0.25 mag scale, as indicated to the right of the profiles. The central region of the profile equivalent to the size of the seeing was not plotted. We did not apply deconvolution in these profiles, for the gain in information would not be significant.

clusters presented here are divided into two groups (Searle et al. 1980): types II-III are rich in red supergiant and AGB luminous stars, which dominate its infrared colors; in types IV-VI, the contribution of AGB stars is still stronger, especially that of carbon stars.

We can see that the integrated colors of the galaxies of our sample, with some exceptions, are compatible with populations like those found in the more metal-rich clusters of the Andromeda galaxy and of our own Galaxy. In all cases, populations like those found in extremely red clusters of the Magellanic Clouds, which are dominated by giant stars of the asymptotic branch, can be ruled out. For galaxies NGC 7192, NGC 7562 and NGC 7619, the infrared colors are dominated by less metal-rich populations, compatible with the average colors of globular clusters of the Galaxy.

5. Discussion

Here we present a case-by-case analysis of the behavior of the objets of our sample, giving special attention to the objects that show more evidence of peculiarity.

The galaxy that presents the highest effective radius in JHK_s – IC 5105 – has one of the highest deviations between effective radii in infrared and B bands. This galaxy is the most luminous object in our sample. It presents slightly boxy isophotes, and shows small color gradients. These features seem to indicate that its population distribution is homogeneous throughout the radius; the infrared integrated colors are dominated by stellar populations type IV-VI, most influenced by the contribution of AGB carbon stars.

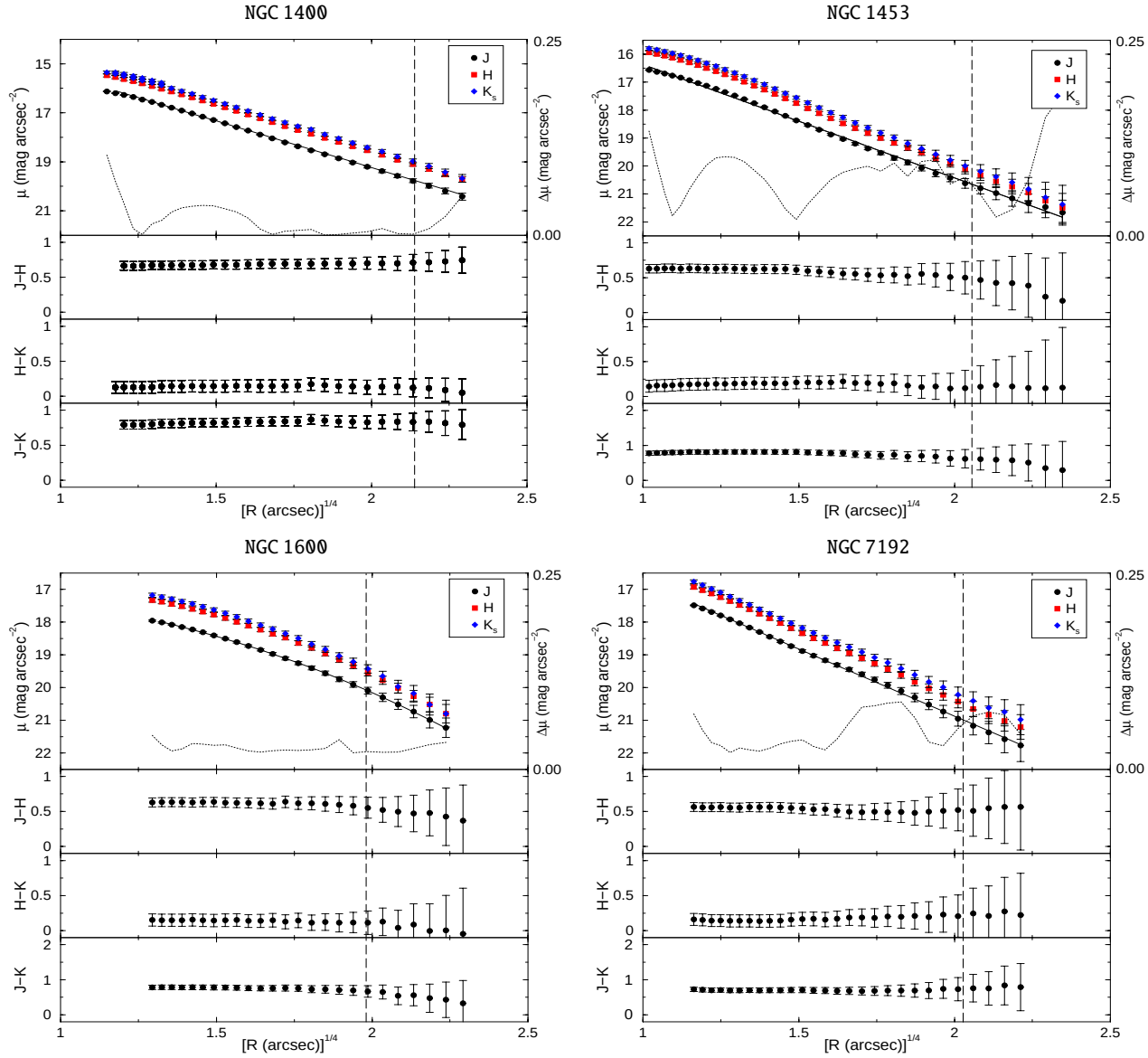

Fig. 2. continued.

Galaxy NGC 7562 shows a similar behavior. Like IC 5105, it presents very similar effective radii in JHK_s and B, and it has the second highest infrared effective radius. In the flux rate diagram, it is located in a bluer-than-average J/H region. So, a contribution of a less metal-rich population is more likely to be present in its infrared colors. This galaxy has a physical companion, NGC 7562A, 2.3 arcmin away.

NGC 1400 shows the smallest effective radius of the sample, and is also the less luminous. This galaxy is a member of a physical association of galaxies (NGC 1407 being the most important) where it is the second most luminous. Its order 3 coefficients present an almost monotonic growth, which can indicate regions of high extinction. It is classified as lenticular, despite the fact that a de Vaucouleurs law fits very well its brightness profile. In relation to the Fundamental Plane, it is the object farthest from the average behavior of the sample.

The galaxy NGC 1600, whose brightness profiles were very well fitted by Sérsic's law, presents the highest effective radius in B compared to the JHK_s ones, indicating that its infrared-dominating stellar population is concentrated in the central region of the galaxy. This galaxy presents boxy isophotes, being the brightest galaxy of a physical association. NGC 720 has also a profile fitted by Sérsic's law (albeit not as well as the former). The central region of the profiles of this galaxy is responsible for the major deviation of the applied laws, being very planar; taking this region (which extends up to 10″) off the profile, the de Vaucouleurs law fits very well. But we see that its isophotes are disky in this very region, becoming boxy in the external region; this is a strong evidence of the presence of a stellar disk in the central region. Goudfrooij et al. (1994), using BVI photometry, also arrived at this conclusion. Note that in the two cases where it was necessary to apply Sérsic's law, the value of the n parameter was lower than 4 (1.5 and 1.8 for

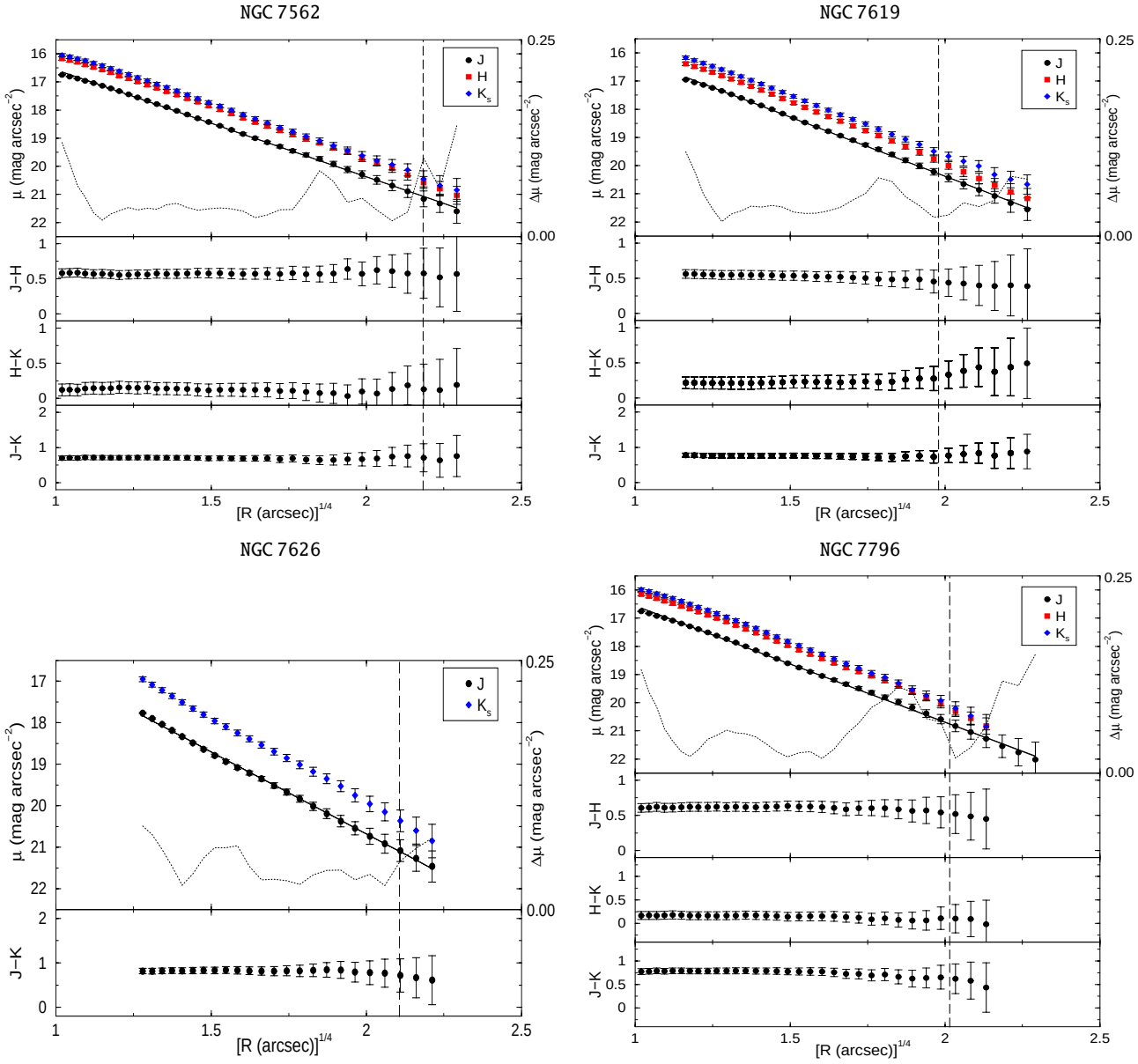

Fig. 2. continued.

NGC 1600 and NGC 720, respectively), indicating that these two objects have a brightness profile more compact than the profiles of the rest of the sample galaxies, well fitted by the de Vaucouleurs law.

Abrupt variations of position angle (more than 40°) ocurred in the galaxies NGC 596, NGC 636 and NGC 7626. The first presents very low ellipticity, which means that, at least in part, the variation of the position angle can be spurious. NGC 636 shows slightly disky isophotes. In both objects, we can see strong and nonconstant variations in the Fourier coefficients; Michard & Marchal (1994), through *V* photometry, proposed for both objects a disk structure in the internal region. For NGC 596, Goudfooij et al. (1994) found the same result. Ferrari et al. (1999) found, for NGC 636, a conical axisymmetrical distribution of dust. Ionized gas in the form of a small internal disk, perpendicular to the orientation of the dust cone, was also found for this galaxy (Macchetto et al. 1996).

The galaxies NGC 7192, NGC 7562 and NGC 7619 are the most displaced with respect to the average in the flux ratios diagram. Its infrared colors are likely to be compatible with the average Galactic clusters population. NGC 7619 is a member of Pegasus I cluster, being the brightest component, followed by NGC 7626. Both present disky isophotes and abrupt variations of A3 and B3 coefficients, possibly indicating high extinction regions. Forbes & Thomson (1992) found evidence of tidal interactions between these two galaxies; since these interactions can induce star formation bursts, this could explain, at least in part, the fact that its infrared colors are among the bluest of our sample.

Table 2. Fitting parameters of brightness profiles. Objects with the symbol (*) have fittings of comparatively minor quality. Galaxies separated by a line at the end of table were fitted with Sérsic's law.

Galaxy	Band	μ_e(mag arcsec^{-2})	R_e(arcsec)	R_e(kpc)	n
IC 5105	J	21.01 ± 0.04	19.33 ± 0.40	10.55 ± 0.21	4
	H	20.38 ± 0.03	20.81 ± 0.44	11.36 ± 0.24	”
	K_s	20.01 ± 0.05	18.12 ± 0.55	9.89 ± 0.30	”
NGC 596	J	20.22 ± 0.03	13.81 ± 0, 22	2.77 ± 0.05	”
	H	19.34 ± 0.03	11.62 ± 0.19	2.33 ± 0.04	”
	K_s	19.27 ± 0.03	12.14 ± 0.22	2.43 ± 0.05	”
NGC 636	J	20.41 ± 0.06	12.78 ± 0.38	2.49 ± 0.07	”
	K_s	19.77 ± 0.07	13.86 ± 0.55	2.71 ± 0.11	”
NGC 1400	J	19.84 ± 0.04	21.23 ± 0.44	1.03 ± 0.02	”
	H	19.31 ± 0.02	23.64 ± 0.31	1.15 ± 0.01	”
	K_s	19.10 ± 0.04	22.37 ± 0.47	1.09 ± 0.02	”
NGC 1453*	J	20.63 ± 0.05	17.70 ± 0.52	7.22 ± 0.21	”
	H	19.70 ± 0.04	14.07 ± 0.34	5.74 ± 0.14	”
	K_s	19.47 ± 0.05	13.61 ± 0.38	5.55 ± 0.15	”
NGC 7192	J	20.99 ± 0.04	16.90 ± 0.35	4.79 ± 0.09	”
	H	20.38 ± 0.02	16.20 ± 0.20	4.60 ± 0.06	”
	K_s	20.38 ± 0.02	17.96 ± 0.22	5.09 ± 0.06	”
NGC 7562	J	21.09 ± 0, 03	22.95 ± 0.46	8.90 ± 0.18	”
	H	20.47 ± 0.04	22.27 ± 0.54	8.64 ± 0.21	”
	K_s	20.37 ± 0.03	22.63 ± 0.42	8.78 ± 0.17	”
NGC 7619	J	20.29 ± 0.03	15.37 ± 0.29	6.25 ± 0.12	”
	H	19.53 ± 0.05	13.21 ± 0.33	5.37 ± 0.13	”
	K_s	19.61 ± 0.02	16.13 ± 0.22	6.56 ± 0.09	”
NGC 7626	J	21.10 ± 0.04	19.76 ± 0.46	7.22 ± 0.17	”
	K_s	20.07 ± 0.04	17.27 ± 0.36	6.31 ± 0.13	”
NGC 7796*	J	20.74 ± 0.04	16.31 ± 0.40	5.38 ± 0.13	”
	H	19.99 ± 0, 04	14.83 ± 0.52	4.88 ± 0.17	”
	K_s	19.34 ± 0.14	10.68 ± 0.80	3.52 ± 0.26	”
NGC 720*	J	19.34 ± 0.12	16.88 ± 1.37	2.95 ± 0.24	1.80 ± 0.32
	H	18.70 ± 0.12	16.84 ± 1.36	2.95 ± 0.24	1.82 ± 0.32
	K_s	18.49 ± 0.12	16.00 ± 1.25	2.80 ± 0.12	1.77 ± 0.30
NGC 1600	J	19.97 ± 0.15	14.62 ± 1.33	7.16 ± 0.65	1.65 ± 0.51
	H	19.11 ± 0.15	12.64 ± 1.05	6.19 ± 0.52	1.45 ± 0.41
	K_s	18.84 ± 0.16	11.70 ± 0.95	5.73 ± 0.46	1.34 ± 0.38

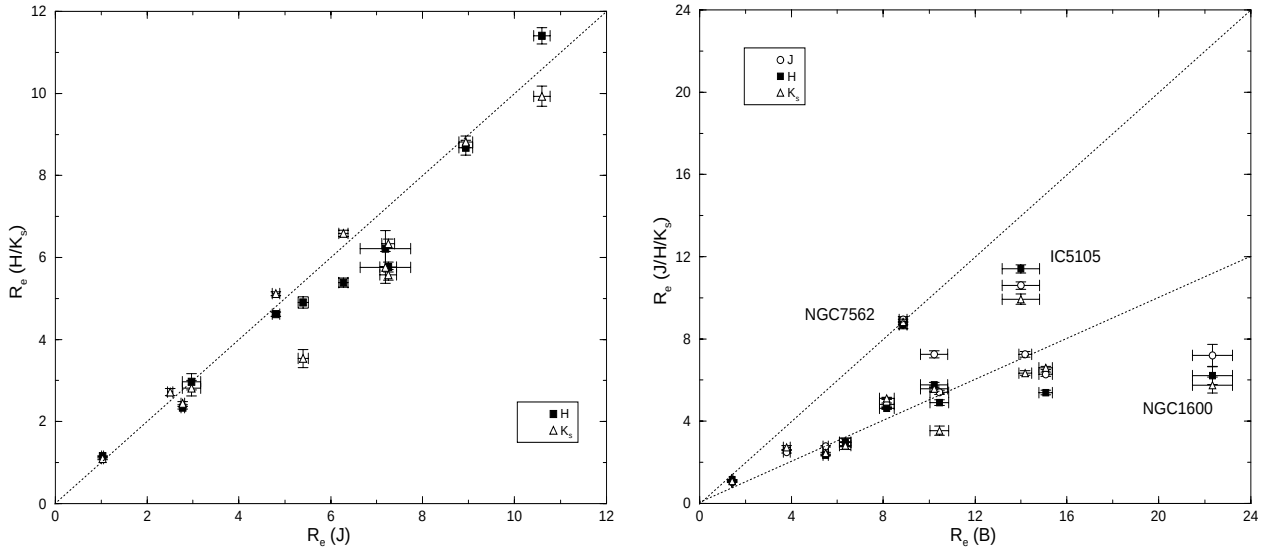

Fig. 3. *left*: comparison between $R_e(J)$ and $R_e(H,K_s)$; *right*: comparison between $R_e(B)$ and $R_e(J, H, K_s)$. Open circles are referred to J, solid boxes to H and open triangles to K_s.

Table 3. Integrated magnitudes and isophotal radii. Objects whose bands are marked by (*) had its observed profiles extrapolated up to the isophotal brightness. The last columns show the integrated magnitude up to a radius of isophotal limit 1 mag brighter than the isophotal magnitude.

Galaxy	Band	$m(0.2{\cdot}R_e)$	$m(0.5{\cdot}R_e)$	$m(R_e)$	m_{iso}	R_{iso} ($''$)	M_{iso}	$\Delta\mu$(mag/arcsec^2)	R^*_{iso}($''$)	m^*_{iso}
IC 5105	$J*$	11.32	10.51	10.07	9.99	34.44	−24.53	0.1	18.57	9.57
	$H*$	10.53	9.74	9.33	9.27	30.32	−25.25	0.4	21.41	8.91
	K_s	10.53	9.67	9.24	9.08	28.36	−25.44	-	17.59	8.87
NGC 596	$J*$	11.43	10.38	9.86	9.52	30.02	−22.83	0.2	19.60	9.25
	$H*$	10.99	9.91	9.37	8.93	29.25	−23.42	0.1	19.45	8.65
	K_s	10.80	9.73	9.19	8.81	25.82	−23.54	-	16.95	8.48
NGC 636	J	11.71	10.71	10.23	9.93	25.71	−22.36	-	17.02	9.65
	K_s	10.80	9.86	9.41	9.18	24.02	−23.11	-	15.59	8.86
NGC 720	$J*$	10.89	9.69	9.15	8.69	52.36	−23.37	0.7	34.64	8.47
	$H*$	10.22	9.03	8.48	8.04	53.14	−24.02	0.5	36.62	7.82
	K_s*	10.15	8.93	8.38	7.97	45.70	−24.09	0.5	30.45	7.77
NGC 1400	J	10.43	9.68	9.30	9.05	50.06	−20.22	-	35.74	8.87
	$H*$	9.67	8.95	8.60	8.36	60.08	−20.91	0.1	40.20	8.21
	K_s	9.58	8.84	8.49	8.26	50.98	−21.01	-	33.29	8.09
NGC 1453	$J*$	11.02	10.21	9.80	9.55	35.45	−24.34	0.3	20.97	8.88
	H	10.67	9.75	9.29	8.96	30.79	−24.93	-	20.28	8.23
	K_s	10.54	9.60	9.14	8.84	26.69	−25.05	-	17.08	8.11
NGC 1600	$J*$	12.15	10.77	10.11	9.70	32.63	−24.59	0.7	22.88	9.45
	$H*$	11.73	10.27	9.55	9.10	27.98	−25.19	0.7	22.67	8.78
	K_s*	11.67	10.19	9.44	9.01	22.59	−25.28	0.2	19.08	8.62
NGC 7192	$J*$	11.53	10.58	10.07	9.86	26.77	−23.24	0.2	16.72	9.55
	$H*$	11.06	10.11	9.60	9.34	26.82	−23.76	0.3	16.88	8.96
	K_s	10.73	9.83	9.36	9.22	23.99	−23.88	-	14.91	8.87
NGC 7562	$J*$	10.92	10.11	9.70	9.56	32.09	−24.22	0.5	21.53	9.22
	H	10.39	9.57	9.16	9.01	33.18	−24.77	-	22.17	8.72
	K_s*	10.24	9.43	9.01	8.88	30.31	−24.90	0.2	19.41	8.51
NGC 7619	$J*$	11.20	10.26	9.80	9.51	32.39	−24.38	0.5	21.05	9.26
	$H*$	10.83	9.83	9.35	9.00	30.96	−24.89	0.3	20.12	8.77
	K_s*	10.35	9.46	9.02	8.77	29.93	−25.12	0.1	19.63	8.47
NGC 7626	$J*$	11.26	10.39	9.92	9.72	29.47	−23.93	0.6	19.45	9.27
	K_s*	10.64	9.75	9.25	9.05	25.63	−24.60	0.1	16.68	8.62
NGC 7796	J	11.37	10.49	10.00	9.78	27.50	−24.51	-	18.47	9.51
	$H*$	10.88	9.94	9.43	9.17	27.02	−25.12	0.6	18.43	8.91
	K_s*	10.95	10.06	9.48	9.06	21.77	−25.23	0.1	15.97	8.64

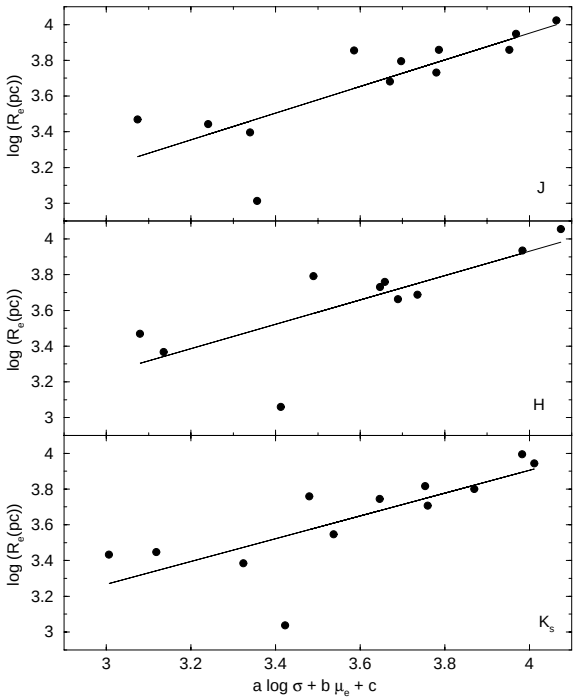

Fig. 4. Edge-on views of the Fundamental Plane for J, H and K_s.

6. Conclusions

The main results found in this work can be summarized as follows:

1. The brightness profiles for most objects of our sample are well fitted by the de Vaucouleurs law.
2. The infrared effective radii of the galaxies of our sample are typically one half of its corresponding radius in B band; this can be interpreted in the sense that the stellar population dominating the near-infrared emission is more concentrated that the bluer population.
3. The color gradients found are very small, and show a general trend toward bluer colors in the external region.
4. The infrared colors of the sample are compatible with stellar populations such as those found in metal-rich Galactic clusters. The galaxies NGC 7192, NGC 7562 and NGC 7619 are compatible with less metal-rich populations.
5. The infrared effective radius (R_e) and the effective brightness (μ_e) of the sample galaxies confirm the Fundamental Plane relation of elliptical galaxies; the rms scatter of the FP is 0.20 dex for J and H, and 0.23 dex for K_s. The a values (slope in $\log\sigma$) are compatible with the general values found in the literature, while b (slope in μ_e) is higher by about 20%.

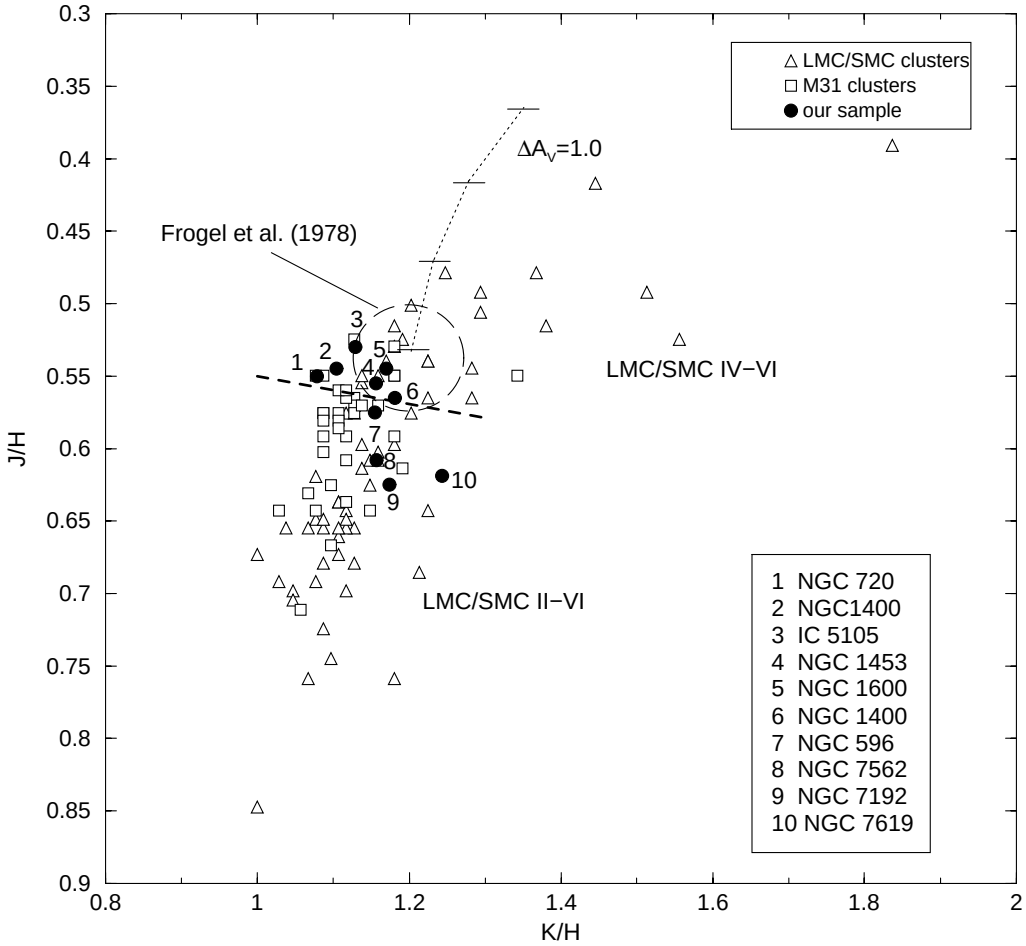

Fig. 5. Flux ratios from integrated isophotal colors compared to globular clusters. Beneath the dashed line, types II-III clusters are concentrated; types IV-VI are scattered by the whole diagram, but are more concentrated above the dashed line. The dashed circle indicates the average colors of the sample of E/S0 galaxies from Frogel et al. (1978).

Acknowledgements. The authors acknowledge CNPq and PRONEX/FINEP 76.97.1003.00 for financial support.

References

Aaronson, M., Cohen, J., Mould, J., et al. 1978, ApJ, 223, 824
Bertola, F. 1981, Sky Telesc., 61, 380
Bender, R., & Moellenhoff, C. 1987, A&A, 177, 71
Binney, J., & Petrou, M. 1985, MNRAS, 214, 449
Caon, N., Capaccioli, M., & D'Onofrio, M. 1993, MNRAS, 265, 1013
de Vaucouleurs, G., de Vaucouleurs, A., Corwin, H. G., et al. 1991, Third Reference Catalog of Bright Galaxies (Springer-Verlag: New York)
Djorgovski, S., & Davis, M. 1987, ApJ, 313, 59
D'Onofrio, M., Capaccioli, M., & Caon, N. 1994, MNRAS, 271, 523
Ducati, J. R., Bevilacqua, C. M., Rembold, S. B., et al. 2001, ApJ, 558, 309
Ferrari, F., Pastoriza, M. G., Macchetto, F., & Caon, N. 1999, A&AS, 136, 269
Forbes, D. A., & Thomson, R. C. 1992, MNRAS, 254, 723
Frogel, J. A., Persson, S. E., Aaronson, M., & Matthews, K. 1978, ApJ, 220, 75
Frogel, J. A., Persson, S. E., & Cohen, J. G. 1980, ApJ, 240, 785
Galaz, G. 2000, AJ, 119, 2118
Goudfrooij, P., Hansen, L., Jorgensen, H. E., et al. 1994, A&AS, 104, 179
Hunt, L. K., Malkan, M. A., Rush, B., et al. 1999, ApJS, 125, 349
Jedrzejewski, R. I., Davies, R. L., & Illingworth, G. D. 1987, AJ, 94, 1508
Kormendy, J., & Djorgovski, S. 1989, ARA&A, 27, 235
Kraan-Korteweg, R. C. 1986, A&AS, 66, 255
Macchetto, F., Pastoriza, M., Caon, N., et al. 1996, A&AS, 120, 463
Michard, R., & Marchal, J. 1994, A&AS, 105, 481
Mihalas, D., & Binney, J. 1981, Science, 214, 829
Milvang-Jensen, B. 1997, Master's Thesis, University of Copenhagen
Mobasher, B., Guzman, R., Aragon-Salamanca, A., et al. 1999, MNRAS, 304, 225
Pahre, M. A., de Carvalho, R. R., & Djorgovski, S. G. 1998, AJ, 116, 1606
Peletier, R. F., Davies, R. L., & Illingworth, G. D. 1990, AJ, 100, 1091
Persson, S. E., Aaronson, M., & Cohen, J. G., 1983, AJ, 266, 105
Persson, S. E., Murphy, D. C., Krzeminski, W., et al. 1998, AJ, 116, 2475
Prugniel, P., & Simien, F. 1996, A&A, 309, 749
Sandage, A., & Tamman, G. A. 1987, A Revised Shapley-Ames Catalog of Bright Galaxies (2nd ed.) (Carnegie Institution of Washington Publication, Washington)
Saraiva, M. F., Ferrari, F., & Pastoriza, M. G. 1999, A&A, 350, 399
Searle, L., Wilkinson, A., & Bagnuolo, W. G. 1980, ApJ, 239, 803
Schlegel, D. J., Finkbeiner, D. P., & Davis, M. 1998, ApJ, 500, 525
Scodeggio, M., Gavazzi, G., Belsole, E., et al. 1998, MNRAS, 301, 1001
Tamura, N., Kobayashi, C., Arimoto, N., et al. 2000, AJ, 199, 2134